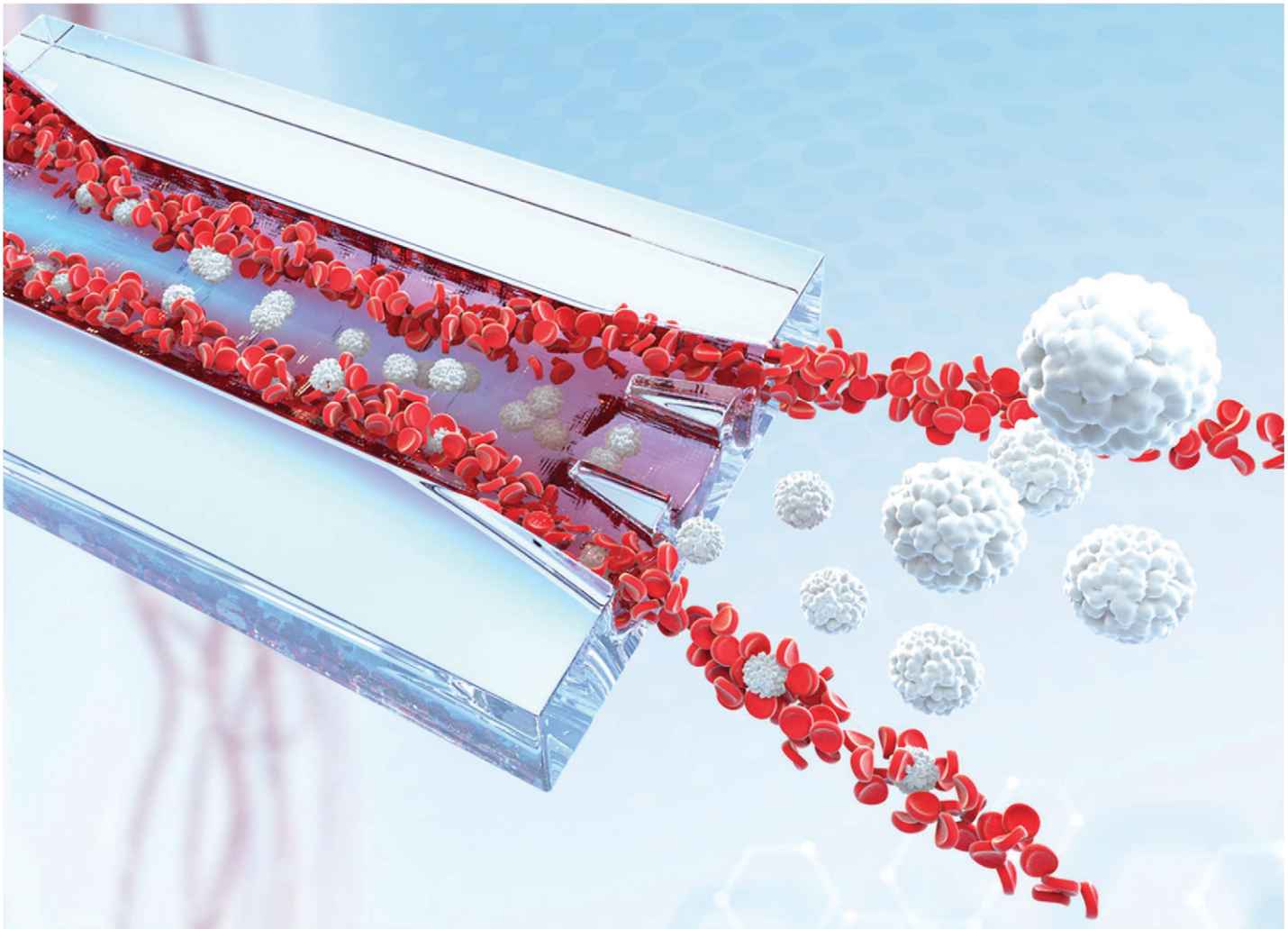

Showcasing research from Professor Ian Papautsky's laboratory, Department of Bioengineering, University of Illinois at Chicago. Image credit: Kaya Yasar at Spherical Chicken Studios.

Size-dependent enrichment of leukocytes from undiluted whole blood using shear-induced diffusion

Size-dependent lateral migration of cells in flow of untreated whole blood is demonstrated and successfully applied to enrichment of leukocytes from whole blood. High-speed imaging revealed migration in blood flow under the influence of shear-induced diffusion. These new insights improve understanding of this counterintuitive phenomenon, offering the possibility of enrichment and separation of cells directly from undiluted whole blood.

As featured in:

See Jian Zhou and Ian Papautsky, *Lab Chip*, 2019, **19**, 3416.

ROYAL SOCIETY OF CHEMISTRY | Celebrating IYPT 2019

rsc.li/loc

Registered charity number: 207890

Lab on a Chip

PAPER

View Article Online
View Journal | View Issue

Cite this: *Lab Chip*, 2019, **19**, 3416

Size-dependent enrichment of leukocytes from undiluted whole blood using shear-induced diffusion†

Jian Zhou [ab] and Ian Papautsky [*ab]

Received 9th August 2019,
Accepted 26th August 2019

DOI: 10.1039/c9lc00786e

rsc.li/loc

Little work has been done in microfluidics with separation of cells directly from whole blood, and the handful of microfluidic systems reported the literature offer only limited throughput. Yet high throughput is highly desirable to avoid degradation of samples, which can result in loss of information critical to disease diagnosis or monitoring. In this work, we investigated particle migration dynamics in whole blood flow at a single-particle level and subsequently successfully demonstrated the preferential enrichment of white blood cells (WBCs) in unprocessed whole blood flows flanking a buffer flow. Our in-depth investigation reveals a counter-intuitive, size-based migration of cells in whole blood flow and their tendency to accumulate in the regions near flow interfaces, which is employed for inherent enrichment of WBCs. More importantly, we found the strong size-dependent migration in blood flow stemming from the differentiated downstream velocity of particles, which inversely scales with particle size. Our new insights improve understanding of this counterintuitive microfluidics field, offering guidance for new device design to directly handle whole blood and to expand the applications to meet the real-world need for ultra-fast cell separation.

Introduction

Blood analysis is one of the most commonly performed clinical tests.[1,2] Obtaining target cellular components in a timely manner is crucial as biosamples can degrade and lose information critical to disease diagnosis or monitoring. Thus, cell separation techniques must be capable of high throughput; one example is liquid biopsy which includes isolation of a small number of circulating tumor cells (CTCs) from a 7.5 mL blood draw.[3] Microfluidic techniques have rapidly emerged as viable alternatives to the conventional benchtop methods for such applications.[4–6] Electric,[7] magnetic,[8] acoustic[9] and optical[10] forces are often introduced into microfluidic systems for accurate manipulation of cells in such separation systems. On the other hand, microfluidic systems without external forces, such as deterministic lateral displacement (DLD),[11,12] pinched flow fractionation (PFF),[13,14] hydrodynamic filtration,[15,16] viscoelastic focusing,[17,18] and inertial microfluidics[19–21] are also bourgeoning, with the latter receiving particular attention due to considerably higher throughput and simplicity.[22,23] Nevertheless, these techniques, and especially inertial microfluidics, require a 5–100× dilution, which effectively creates an upper limit on the throughput. Eliminating dilution and working with whole blood directly is thus highly desirable.

Little work has been done in microfluidics with whole blood to date, and the handful of microfluidic systems reported in literature offer only limited throughput. These methods are generally based on principles of cell margination,[24,25] cross-flow filtration,[26,27] and DLD.[28,29] Separation of cells using cell margination is however not practical due to low throughput (nL min^{-1}). Addition of contraction-expansion units to straight microchannel can increase it to 5 μL min^{-1} for cell separation.[30] While cross-flow filtration devices offer higher throughput (17 μL min^{-1}), the separation efficiency (27% continuously[26] and 72% discontinuously[27]) critically limit applications targeting rare cells. In addition to

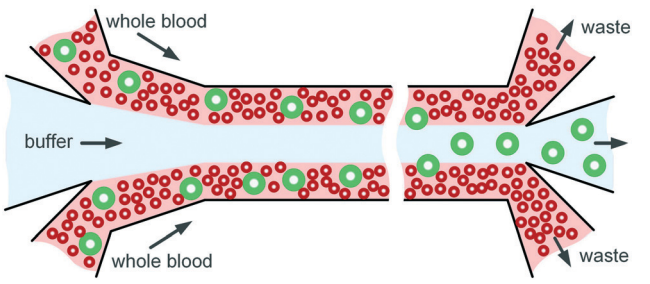

Fig. 1 Schematic of the flow configuration. Whole blood sample flow is separated by a central stream of PBS buffer. Particles (green) suspended in whole blood migrate toward the channel center despite interactions with blood cells (red).

[a] *University of Illinois Cancer Center, Chicago, IL 60612, USA*
[b] *Department of Bioengineering, University of Illinois at Chicago, 851 S. Morgan Street, 218 SEO, Chicago, IL 60607, USA. E-mail: papauts@uic.edu; Tel: +1 312 413 3800*

† Electronic supplementary information (ESI) available. See DOI: 10.1039/c9lc00786e

lateral displacement, tapered post microarray coupled with cell deformability, and a microchannel with ridges on top wall were also used in separation of blood, but their efficiencies remain below 80%.[31,32] Better performance was reported in a spiral channel with trapezoid cross-section.[33]

Recently we reported a new method using co-flow microfluidic system[34] that offers high efficiency (>90%) and high throughput (10^6–10^7 cells per s) for untreated whole blood, exceeding that of the ultra-fast inertial devices.[35] The separation principle of this device, schematically shown in Fig. 1, is based on lateral migration of particles and cells in whole blood, which previously was thought to be impossible. We successfully demonstrated direct isolation of CTCs from patient peripheral whole blood without sample preparation.[35] While the new approach shows superior performance, the underlying mechanism remains poorly understood. The migration is in the opposite direction of margination effect.[24,25] We proposed the shear-induced diffusion (SID)[34] as the migration mechanism, since inertial migration is excluded due to the numerous cell–cell interactions in whole blood.[36,37] The viscoelasticity of whole blood is generally weak[38] (Weissenberg number, a dimensionless parameter used to measure fluid elasticity, Wi < 1) and thus its effect on particle migration is considered to be minor despite co-flow of non-Newtonian and Newtonian fluids was reported for particle separation.[39–41] In this earlier work, the size-dependent lateral migration of cells in whole blood was investigated using fluorescent streak velocimetry of stained cells and particles, which showed collective behavior. However, the exact principle of migration in whole blood flow remains unclear. To develop an understating of this counter-intuitive phenomenon, we must first analyze migration dynamics of individual particles in whole blood.

In this work, we investigate the migration dynamics of particles in whole blood at single-particle level using high-speed imaging, and observe lateral migration through trajectories of individual particles, which is subsequently utilized for successful enrichment of WBCs inside whole blood directly. Surprisingly, we find that downstream velocity of particles, which is inversely related to particle size, is the main contributor to the size-dependent focusing observed previously through fluorescent streak velocimetry. Due to their larger size in blood flow, WBCs migrate faster toward the channel center, leading to inherent enrichment of WBCs at high throughput. We believe these findings shed light on the migration dynamics in complex cellular suspensions, which in turn improves understanding of dynamics in microfluidic systems toward the next-generation technology of cell separations.

Experimental methods

Microchannels were fabricated *via* standard soft photolithography. Briefly, negative photoresist (SU-8 2050, MicroChem Corp.) was used to pattern microchannels on a 3″ silicon wafer by conventional photolithography. Polydimethylsiloxane (PDMS, Sylgard 184) was cast on the wafer and peeled after 6 hour curing on 65 °C hotplate. Replicated straight channels (120 μm wide × 45 μm high) in PDMS were bonded to 1″ × 3″ glass slides (Fisher Scientific) using oxygen plasma surface treatment (PE-50, Plasma Etch Inc.). The inlet and outlet ports were punched manually using stainless flat head needles. Sample and buffer solutions were injected into the PDMS device with a dual-syringe pump (Legato 200, KD Scientific Inc.) to sustain stable flow. The loaded syringe was connected to 1/16″ Tygon® tubing (Cole-Palmer, Inc.) using proper fittings (IDEX Health & Science LLC) and then secured to the device inlets.

Microparticles spiked in whole bovine blood were used to demonstrate the lateral migration in our co-flow microchannel. Fresh bovine blood was purchased from Lampire Biological Laboratories and used within 48 h. Four particles with diameters of 15.5 μm (BangsLab), 18.7 μm (Polysciences), 26.3 μm (Polysciences) and 31.2 μm (Spherotech) were spiked into whole blood at volume ratio of 1 : 50. Phosphate-buffered saline (PBS) was used to form the middle stream flanked by blood flows in our co-flow microchannel. Flow rates were fixed at 112.5 μL min^{-1} for both blood and PBS flows, for the total flow rate of 225 μL min^{-1}.

Particle, blood and PBS flows were imaged using a motorized inverted microscope (IX-83, Olympus). The observation window of high-speed camera (Mini AX200, Photron USA) was set to 1024 μm × 128 μm (20× objective). Frame rate was 25 000 fps and exposure time was 1 μs. Trajectories of individual particles in whole bovine blood were obtained by stacking consecutive frames using ImagJ®. Downstream and lateral positions of particles at each frame were measured manually using PFV software (Photron USA).

For WBC enrichment experiments, human blood was purchased from ZenBio, Inc. (Research Triangle Park, NC, USA). These experiments were performed in compliance with the Institutional Review Board (IRB) protocol # 2018-0146. The experiments were performed in a longer channel (150 μm width × 50 μm height × 20 mm length), yielding flow rates of 133 and 267 μL min^{-1} for blood and buffer flows, respectively. To visualize subtypes, WBCs were stained by adding 1 mL acridine orange (0.1 mg mL^{-1}) into 1 mL WBC suspension and incubating for 15 min at room temperature before observation. For flow cytometry tests, whole blood and samples collected from each outlet of the channel were stained by adding 10 μL stock solution of Hoechst 33342 (20 mM) in to 1 mL sample. The samples were kept at 4 °C overnight and then diluted 4–50× before being taken to Flowcytometry Core at University of Illinois at Chicago, where they were processed using CytoFlex cytometry (Beckman Coulter, USA) by a skilled technician. Results were analyzed in Kaluza (Beckman Coulter, USA).

Results and discussion

Lateral migration in whole blood

Tracking particles with high-speed imaging confirms lateral migration in whole blood. In this initial set of experiments,

we imaged the first 1 mm of our co-flow channel where diffusion of RBCs into the PBS stream is minimal.[34] Trajectories of two individual 18.7 μm diameter particles visualized by stacking individual high-speed frames are shown in Fig. 2a and b. These images reveal migration toward the channel center. Particle P1 in the top blood stream laterally displaces toward the channel centerline and the clear PBS stream. Similarly, particle P2 within the bottom blood stream moves upward as it travels downstream. The spacing between particles in each stacked frame increases, indicating increasing downstream velocity.

Measurements of lateral and downstream positions in each frame permit calculation of particle migration velocities (Fig. 2c and d). The downstream velocity was calculated as ratio of the interframe distance and the interframe time span (40 μs). These calculations suggest that the initial particle position significantly affects migration dynamics. Although the two particles entered the straight channel at different lateral positions, their lateral displacements are unexpectedly similar, measuring approximately 8 μm each within the observation window of ~1 mm downstream length. However, the second particle (P2) moved at higher speed downstream since it was initially closer to channel center, suggesting a shorter time for its lateral migration. Our calculation indicates P2 exhibited a faster average lateral migration speed, which was 5 mm s^{-1} as compared to 3.8 mm s^{-1} of P1. These results suggest that lateral migration velocities of particles in whole blood are dependent on their initial transverse positions in our co-flow microchannel. Thus, we next examined the downstream and lateral velocities of particles in more detail.

Lateral migration velocity

Two orthogonal velocities are defined to quantify lateral migration. Since the inter-frame lateral displacement of particles generally is below resolution of the camera, we must calculate the average lateral migration velocity for a fixed time span to allow discernible lateral displacement. This was done over a 300 μm-wide field of view, at approx. 700 μm downstream from entrance, to avoid influence of flow development on particle lateral migration. As a result, the calculated average lateral velocity is termed average local lateral velocity (LLV, denoted as $\overline{U}_l$) to reflect its dependence on the selection of downstream position. Note the time span is dependent on downstream velocity. The corresponding average downstream velocity is then termed as local downstream velocity (LDV, denoted as $\overline{U}_d$).

Measurements of $\overline{U}_l$ and $\overline{U}_d$ confirm the location-dependent migration behavior of particles in whole blood. While the distribution of downstream velocity across the channel width (Fig. 3a) resembles parabolic profile in a single-fluid flow (*e.g.*, Newtonian water flow in a channel), the lateral migration velocity shows a different pattern. For particles close to channel wall, their $\overline{U}_d$ increases as they move

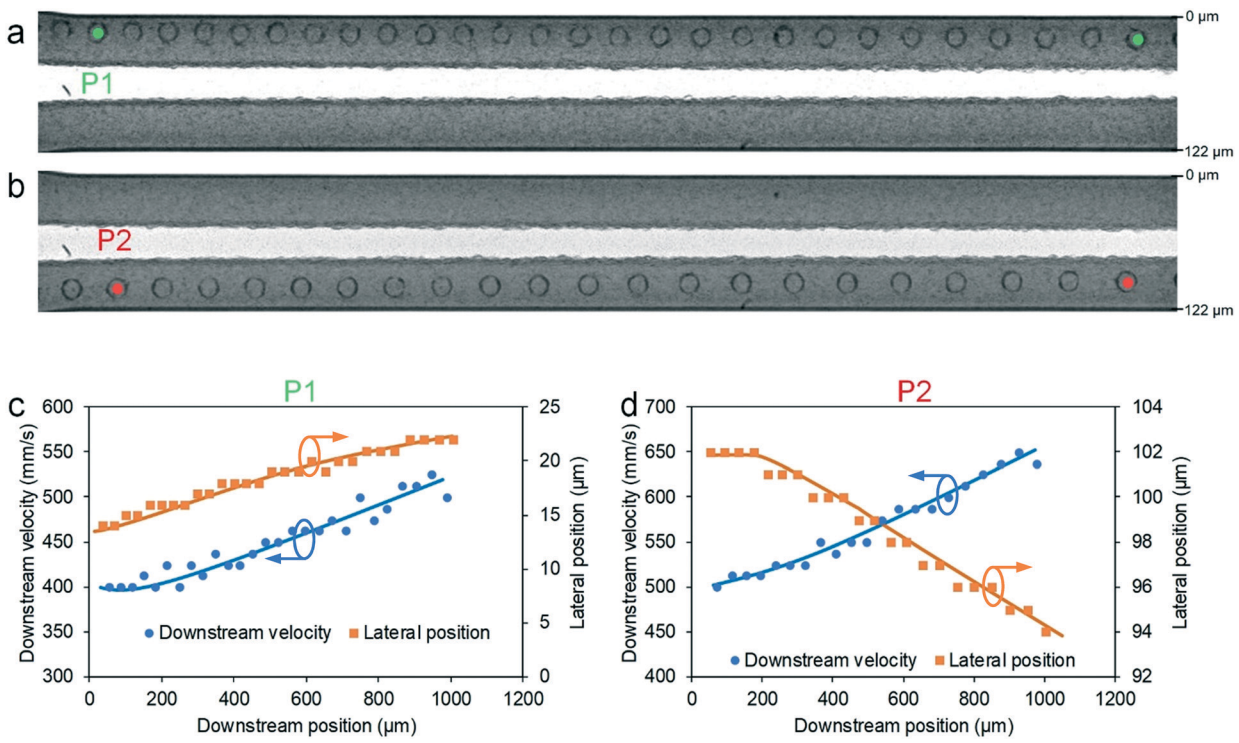

Fig. 2 Lateral migration of particles in whole blood. Migration of particles P1 (a) and P2 (b), both initially located near the channel walls. Composite bright-field images show trajectories of individual 18.7 μm diameter particles. Downstream velocity and lateral position plotted as function of downstream positions for particles P1 (c) and P2 (d). Lateral position was measured from the top wall (0 μm). Red and green spots are for visual guidance. Flow rates were 112.5 μL min^{-1} for both blood and PBS flows. Frame rate was 25 000 fps. Images in (a) and (b) were stacked every two frames for improved visualization.

away from the wall. The $\overline{U}_l$ achieves its maximum at lateral position of approximately 35 μm but declines sharply beyond that (Fig. 3b). When particles are in proximity to the fluid interface of blood and PBS, their lateral velocity is minimal but not necessarily zero. It can be even negative since particles might oscillate around the interfaces. In this work, we define positive migration velocity as migration toward channel center while negative velocity for migration toward channel walls. Plotting $\overline{U}_l$ as a function of $\overline{U}_d$ in Fig. 3c reveals that the negative migration occurs when particle velocity exceeds ~880 mm s^{-1}.

The incoherent migration suggests migration dynamics could be different for particles flowing in the PBS flow flanked by the blood streams. Fig. 4 shows mixed migration behaviors of particles suspended in PBS. As expected, the particle at the fluid interface showed a negative migration with 2–3 μm displacement into blood stream (Fig. 4 and 5a). This small lateral displacement can be an artifact as particles located at interface may experience velocity oscillation (back and forth) as suggested by the small variations of downstream velocity along the course. Particles initially in between the interface and channel center display more complex behaviors. A particle initially close to channel center in Fig. 4 showed small negative migration (3 μm displacement toward interface) and a particle initially near interface on the other hand rapidly moved in the opposite (positive) toward channel center with 6 μm displacement (Fig. 5c). While initial lateral position seems determining the migration direction in this case, particle vertical position may also contribute to such uncertainty in terms of migration direction. We are not able to either confirm or exclude this factor with our current setup.

Another unexpected finding is that particle initially in proximity to the channel center decreased its downstream velocity with almost no lateral displacement (Fig. 5d). Since PBS is a Newtonian fluid, particles are expected to stabilize in the channel center due to the balance of inertial forces.[36] Deceasing in downstream velocity suggests that particles can migrate toward the top or bottom channel walls without lateral velocity. Another possible reason could be due to that the local flow velocity may decline due to interaction of blood and PBS streams. The downstream velocity stopped decreasing when it was around 900 mm s^{-1} which is close to the observed threshold in Fig. 3c (880 mm s^{-1}).

Critical velocity

This coincidence becomes more evident when we aggregate velocity data of particles suspended in PBS and that of particles spiked in whole blood. Now we have full pictures of particle downstream and lateral velocities across the entire channel width (Fig. 6). Similar to particles in blood stream, we also used LDV ($\overline{U}_d$) and LLV ($\overline{U}_l$) in quantifying migration dynamics. The merged data first show a velocity profile resembling parabola which is characteristic of a laminar Newtonian flow (Fig. 6a). Some particles near the fluid interface show higher downstream velocity, which suggests these particles might be located in different vertical positions. Unlike other particles, these possessed negative migration in terms of $\overline{U}_l$ (Fig. 6b). Moreover, no negative migration velocity was observed for particles in blood stream away from the interface. On contrast, some particles in PBS away from the interface also possessed negative lateral velocity (Fig. 6b).

Plotting $\overline{U}_l$ as a function of $\overline{U}_d$ clearly confirms there is a critical downstream velocity which determines the sign (negative or positive) of particle migration velocity. The critical velocity is around 880 mm s^{-1} in this work with a total flow rate of 225 μL min^{-1}. Regardless of particle lateral positions, particles with downstream velocity exceeding the threshold exhibit negative migration directing to channel walls. Considering the 3D velocity profile in a microchannel, fluid velocity is higher in the center-plane in vertical direction and in the centerline in horizontal direction. Particle downstream velocity is also related to fluid speed. Consequently, results in Fig. 6 suggest that particles with negative migration and higher downstream velocity may be located either close to channel center-plane or centerline. In general, particle migration dynamics is more heterogeneous in PBS stream than in blood streams where particles migrate monotonously toward the fluid interface except those close to the interface.

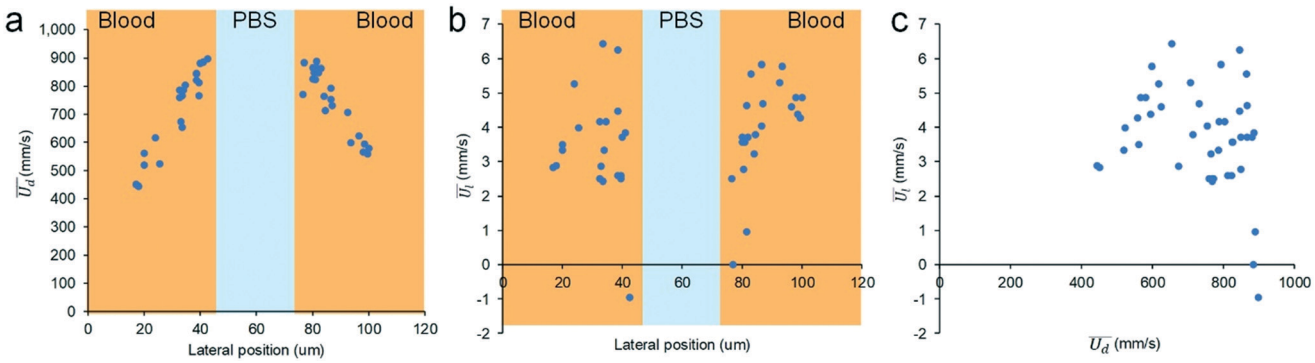

Fig. 3 Migration dynamics in whole blood of 18.7 μm diameter particles. (a) Local downstream velocity ($\overline{U}_d$) as a function of lateral position in the microchannel. (b) Pattern of local lateral velocity ($\overline{U}_l$) across the channel width. (c) Plot of $\overline{U}_l$ as a function of $\overline{U}_d$. Flow rates were 112.5 μL min^{-1} for both blood and PBS flows. A n = 41 of beads were measured.

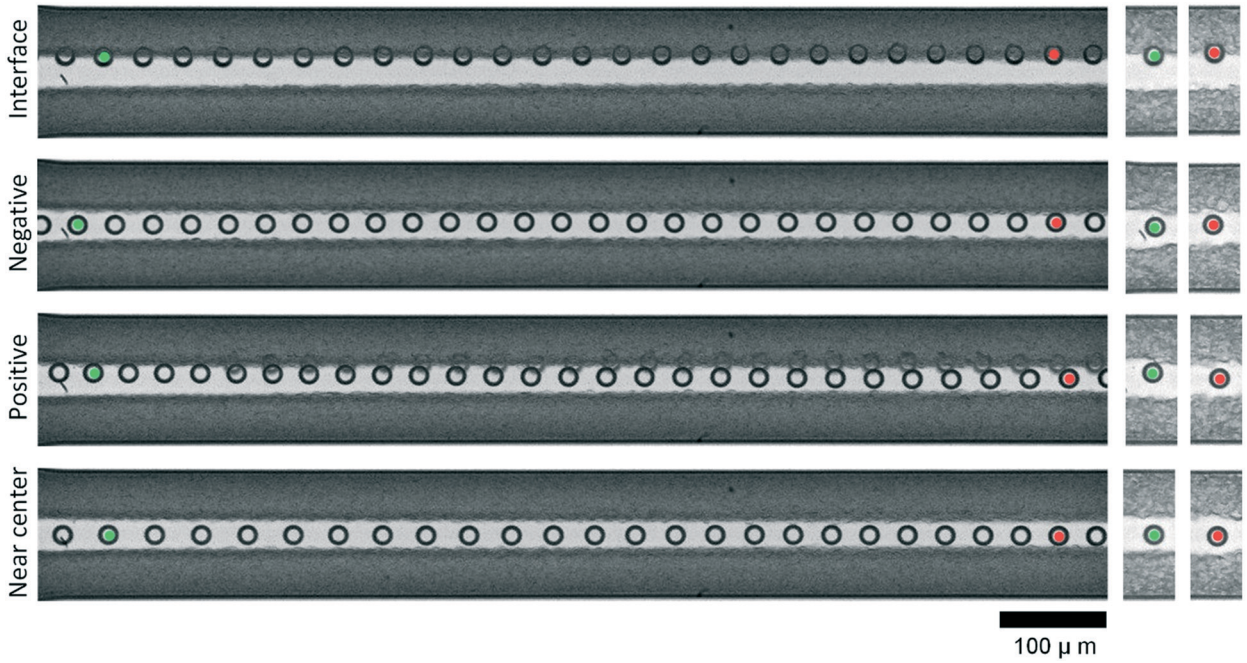

Fig. 4 Migration of particles in the PBS stream flanked by streams of whole blood, illustrating four migration patterns near fluid interface, with off-center (negative) migration, with toward-center (positive) migration and near channel center. Green spots highlight initial lateral positions of the four cases and red spots identify their lateral positions near the end of the observation window. Cropped images of individual frames from high-speed imaging are attached on the right to show lateral displacements of the four particles. Flow rates were 112.5 μL min^{-1} for both blood and PBS flows.

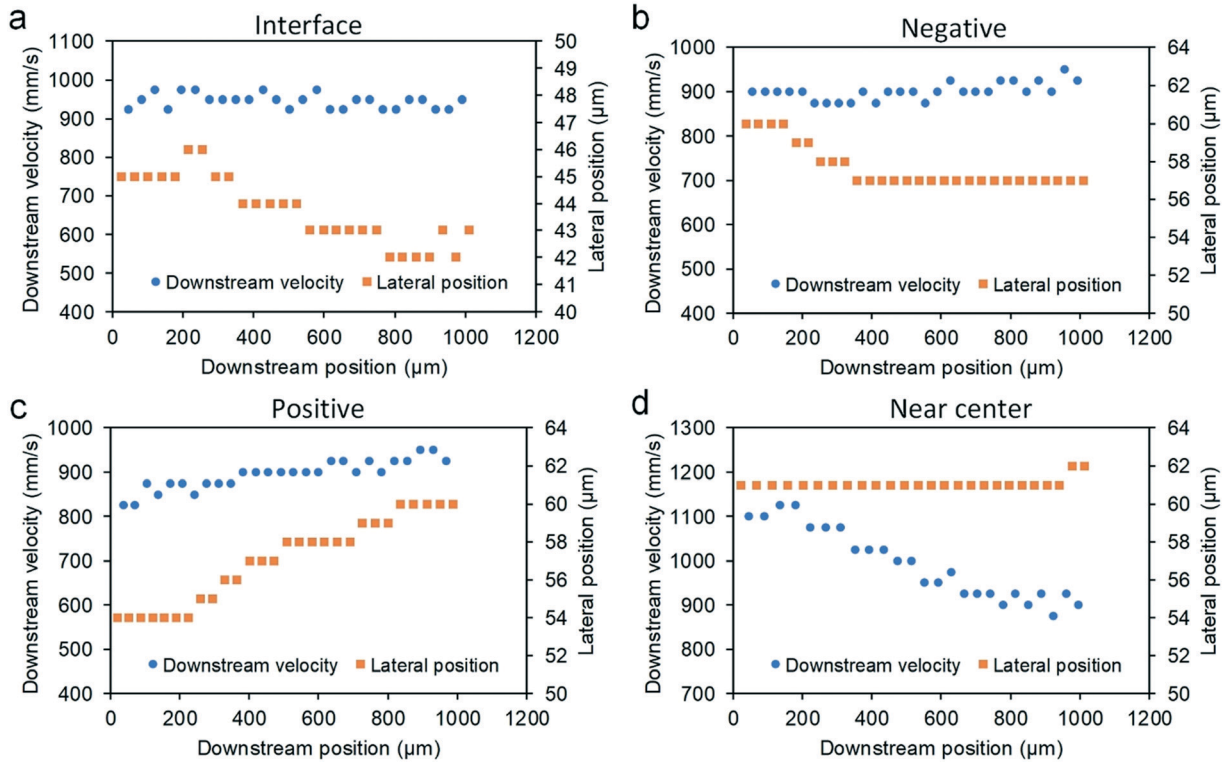

Fig. 5 Quantitative measurements of downstream velocity and lateral position for the four cases displayed in Fig. 4: (a) particle at the interface of blood and PBS stream, (b) particle showing negative migration, (c) particle showing positive migration, and (d) particle near center showing very little migration.

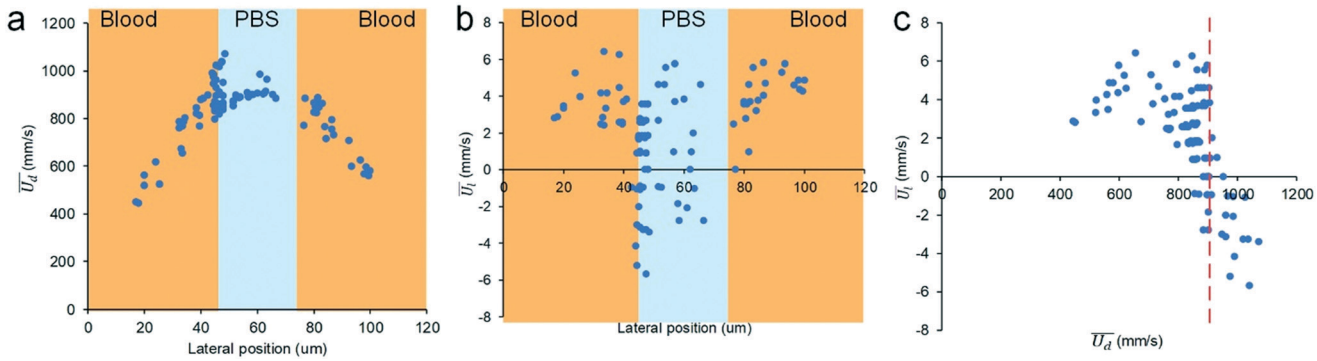

Fig. 6 Migration dynamics of 18.7 μm diameter particles across channel width. (a) Local downstream velocity ($\overline{U}_d$) as a function of lateral position in the microchannel. (b) Local lateral velocity ($\overline{U}_l$) as a function of lateral position in the microchannel. (c) Plot of $\overline{U}_l$ as a function of $\overline{U}_d$. The red dashed line indicates a threshold of ~880 mm s^{-1} $\overline{U}_d$. A total of n = 109 individual particles were measured. Flow rate was 112.5 μL min^{-1} for both blood and PBS flows.

Size-dependent migration

Migration in whole blood exhibits dependence on size, with larger particles migrating faster than the smaller ones, analogous to inertial migration.[36] We investigated this phenomenon by spiking particles of different diameters into whole blood and injecting samples into our system at the same flow rate. The largest particle we used, 31.2 μm in diameter, migrated 14 μm toward the channel center within 1 mm downstream length, while the smallest particle we used, 15.5 μm in diameter, migrated only 6 μm. The displacements for the 26.3 μm and 18.7 μm diameter particles were 10 μm and 7 μm, respectively. Trajectories of these particles are presented in Fig. 7.

Measurements of lateral position as a function of downstream velocity are presented in Fig. 8a. Initially, all four particles were close to channel sidewall. There was a larger gap between 18.7 μm particle and channel wall as compared to other particles. Despite different initial lateral positions due to their physical sizes, Fig. 8a provides critical insight into the size-dependent migration dynamics. The larger particles travel slower downstream than the smaller particles. The curve of interframe downstream velocity of larger particle shifts to upper-left direction as compared to smaller particles. The gap between adjacent curves increases as particle becomes larger. At a given lateral position in Fig. 8a, downstream velocity of smaller particles is much higher than

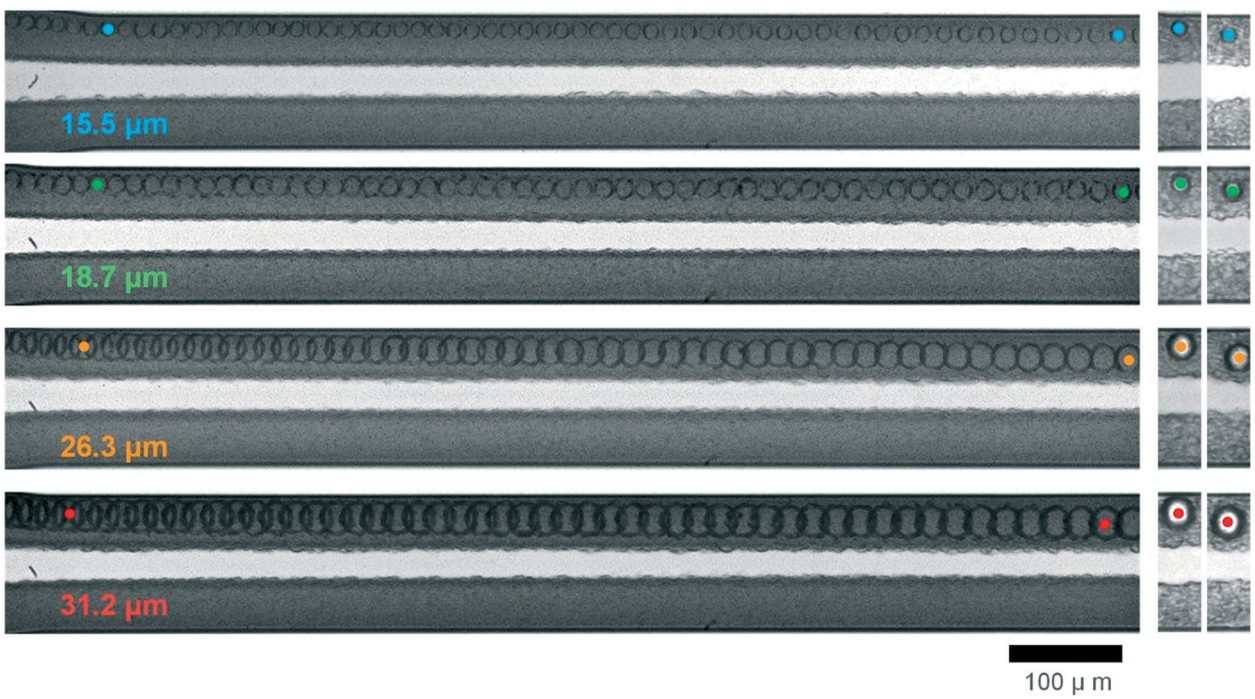

Fig. 7 Demonstration of size-dependent migration of particles in whole blood using high-speed imaging for four particle sizes: 15.5 μm, 18.7 μm, 26.3 μm, and 31.2 μm diameter. Flow rates were 112.5 μL min^{-1} for both blood and PBS flows. These are composite bright-field images showing trajectories of the four individual particles. Colored spots are for visual guidance.

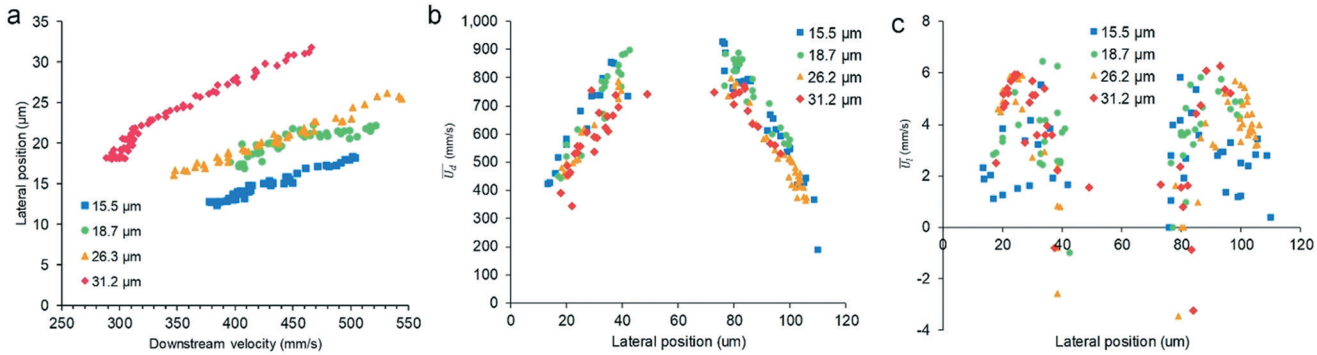

Fig. 8 Size-dependent particle velocities within whole blood flow. (a) Lateral position as a function of downstream velocity for the four individual particles in Fig. 7. (b) Local downstream velocity ($\overline{U}_d$) as a function of lateral position for the four particle sizes. (c) Distributions of local lateral velocity ($\overline{U}_l$). Flow rates were 112.5 μL min^{-1} for both blood and PBS flows.

larger particles if regardless of constrains of particle physical size and if the curves are necessarily projected. Recall that larger particles would also have larger lateral displacement, which leads to uncertainty of lateral migration velocity as slower downstream speed of larger particles means longer residential time for particles traveling through the 1 mm observation window.

This inverse relationship of particle downstream velocity and size is further corroborated by our measurements of $\overline{U}_d$ for large number of particles (Fig. 8b). While some data points appear close to each other, generally, smaller particles have larger $\overline{U}_d$ as those data points are on top of others, with $\overline{U}_d$ of 31.2 μm particles at the bottom. Note no data points close to lateral positions of 0 and 120 were recorded as these are excluded by particle physical size (only lateral positions larger than particle radius are possible).

Unlike the clear distribution of $\overline{U}_d$ of different particles, our measurements of $\overline{U}_l$ show complicated scatter distributions (Fig. 8c). While generally larger particles seem having slightly faster migration velocity, there are large overlap areas. Nevertheless, one trend is quite clear: smaller particles show larger scattering area and their migration velocities varies even at the same lateral positions. On the other hand, larger particles (*e.g.*, 31.2 μm) would have narrower variation of $\overline{U}_l$ for similar lateral positions. Note that the comparison of $\overline{U}_l$ here does not take account of difference of particle vertical positions. Smaller particles have wider range of accessible vertical positions while larger ones do not as their available vertical range is limited by their size. For example, in our 45 μm high channel, 15.5 μm particles can be freely dispersed within 29 μm (height minus diameter) vertical range while it is only 13.8 μm for 31.2 μm particles. As a result, smaller particles show more scattered pattern of $\overline{U}_l$.

Although $\overline{U}_l$ of different particles is closely clustered, the size-based migration is certain in terms of lateral displacement. The displacement in practice is defined by multiplying lateral migration velocity and residential time. The latter is given by the channel length and the downstream velocity. As the downstream velocity decreases by increasing particle size, the residential time for larger particles is longer than that of smaller particles. As a result, lateral displacement of larger particles will be larger for a given channel length, which practically will exhibit phenomenal size-dependent migration as demonstrated in Fig. 7.

Regardless of size difference, $\overline{U}_l$ is approximately 1.1% of $\overline{U}_d$ or less (Fig. 8c). The maximum lateral velocities of all four tested particles are quite close, approximately 6 mm s^{-1} and their corresponding downstream velocities are in the range of 550–850 mm s^{-1}. This maximum speed is observed closer to fluid interface for smaller particles. For instance, 31.2 μm particles reach this peak lateral velocity at lateral position of about 25 μm away the nearest channel wall. Conversely, the position is around 35 μm for the smallest particles (15.5 μm). Such dissimilarity can be attributed to the difference in particle diameter. The sums (40.7 μm and 42.7 μm) of lateral position of peak velocity and particle radius for the two particles are very close to 42 μm which roughly is the position of fluid interface. Larger particles touch the fluid interface earlier and the interaction between particle surface and fluid interface causes the decline in lateral migration velocity.

Dynamics at fluid interface

Oscillatory movement at the fluid interface was observed for different particles, implying distinct migration dynamics (Fig. 8c). Our recently work[34] on cell separation in whole human blood has suggested that shear-induced diffusion (SID) is most likely responsible for the lateral migration of particles and cells in blood. The shear-induced diffusion mainly stems from the irreversible interaction between suspended particles.[42] When particles approach the fluid interface, the interaction mode is disrupted since there is no cell in PBS stream to interact with the particle. The particle only interacts with blood cells on one side. This change may affect the effectiveness of SID.

On the other hand, our simulation results in previous work[34] have shown shear rate across the interface is higher than that in both sides of blood and PBS stream. This high shear rate also contributes to the decline of SID effectiveness since particles directionally migrate to regions of low shear

rate under SID effect. There is another factor that may contribute to negative migration observed across the interface. As shown in Fig. 6, some particles in PBS side also had negative migration velocity which directs from low shear rate region in center of channel cross-section (channel axis) to the interface.[34] This off-center motion suggests shear-induced lift force (one of the inertial forces[37]) takes place in PBS flow and it can counteract the effect of shear-induced diffusion which is in the opposite direction. Shortly, these three factors together may govern the dynamics of particle migration across the fluid interface.

For particles away from the fluid interface in PBS, inertial forces dominate the heterogenous migration observed in Fig. 6b. Since all the particles possessing negative velocity had higher downstream velocity, we infer these particles were vertically close to the channel axis where downstream speed is faster and thus, they migrated away toward channel walls either horizontally or vertically undergoing shear-induced lift force (*e.g.*, Fig. 5b and d). For particles close to top and bottom walls, shear-induced lift force would be balanced with wall-induced lift force and rotation-induced lift force would thus become dominant in particle migration and these particles possess positive migration (*e.g.*, Fig. 5c).[37] Since our camera was observing from the bottom of the microchannel, we are not able to differentiate the vertical positions of particles and thus both positive and negative migration were observed horizontally.

The bi-directional migration in PBS stream and the significantly reduced migration near fluid interfaces suggest that it is difficult for particles in blood stream to migrate into the center of PBS flow. This is unfavored in the cell separation applications. Larger particles and cells will be accumulated at the fluid interfaces if no further change of fluid condition. Nevertheless, we observed focusing of particles and cells in the channel center and even separation of CTCs was demonstrated in our other recent work.[34] This discrepancy is readily reconciled because of the fact that blood cells would also diffuse into PBS stream along with the preferential migration of larger particles. The diffusion of blood cells is slower, but it pushes the fluid interface toward channel center. For example, the 15.5 μm particle in Fig. 7 migrated 7 μm toward channel center, but the corresponding interface only advanced 2 μm. We have shown that whole blood can rapidly diffuse into PBS and cause mixing of blood and PBS, leading to the focused particle stream in channel center.[34] Nevertheless, the diffusion of blood cells may not be preferred as these cells could contaminate the separation outcome.

WBC enrichment in whole blood

The strong size-dependent migration of particles in whole blood suggests inherent preferential redistribution of WBCs inside the blood flow near channel sidewalls. Representative images of WBCs are shown in Fig. 9 where WBC subtypes were fluorescently labeled by Acridine Orange. Monocytes and granulocytes (including neutrophils, basophils and eosinophils) are generally larger than RBCs, while lymphocytes have similar size to RBCs (~7 μm). Lymphocytes roughly constitute 30% of WBCs and the rest is about 70%.[43] Therefore, under SID effect, majority of WBCs migrate toward the PBS flow faster than RBCs, leading to enrichment of WBCs near channel center instead of near sidewalls under the effect of WBC margination.[24,25]

Flow cytometry results of cell counting confirm enrichment of WBCs inside whole blood flow. Adding three outlets as shown in Fig. 1, blood sample were recollected from the central outlet (inner outlet, IO) and the two side outlets (grouped as outer outlet, OO). WBCs were differentiated from RBCs by PB450-H channel (Hoechst 33342 in this work) and subpopulations of WBCs were distinguished through the channel of side scatter height (SSC-H). Fig. 10 shows the SSC-PB450 plots of the results for samples of input, IO and OO. Due to autofluorescence, RBCs were also detected in PB450-H channel, but their fluorescence intensity is lower than that of WBCs in general. The shape variation of RBC population in the three samples were due to their different suspending mediums inducing morphological change of RBCs. Sample collected from IO was significantly diluted in PBS (Fig. 1). More spiky or star-shaped RBCs were observed in this sample after overnight incubation, resulting in broader distribution of RBCs in the scatter plot (Fig. 10). Nevertheless, decrease of lymphocyte concentration is evident in IO sample.

Quantification of blood cells counting demonstrates the preferential lateral migration of WBCs (Fig. 11). The percentage of WBC population, which is defined as WBCs/(WBCs + RBCs), increased from 0.17% in the initial blood sample to 0.44% in IO (Fig. 11a). The percentage decreased to 0.06% in the sample of OO, accordingly. As a result, WBCs indeed migrated faster than RBCs into the central buffer flow, as suggested by the SID effect. The enrichment ratio was 2.6×. Size-dependent migration of WBCs in whole blood is further evidenced in the percentage distribution of the three subpopulations. The percentage of granulocytes including

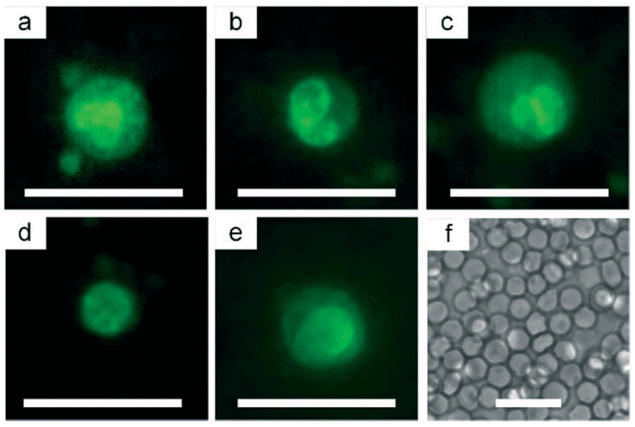

Fig. 9 Representative images illustrating size of WBCs and RBCs. (a) Neutrophil. (b) Basophil. (c) Eosinophil. (d) Lymphocyte. (e) Monocyte. (f) RBCs. All WBCs were stained by acridine orange and pseudocolored green for better visualization. Scale bars represent 20 μm.

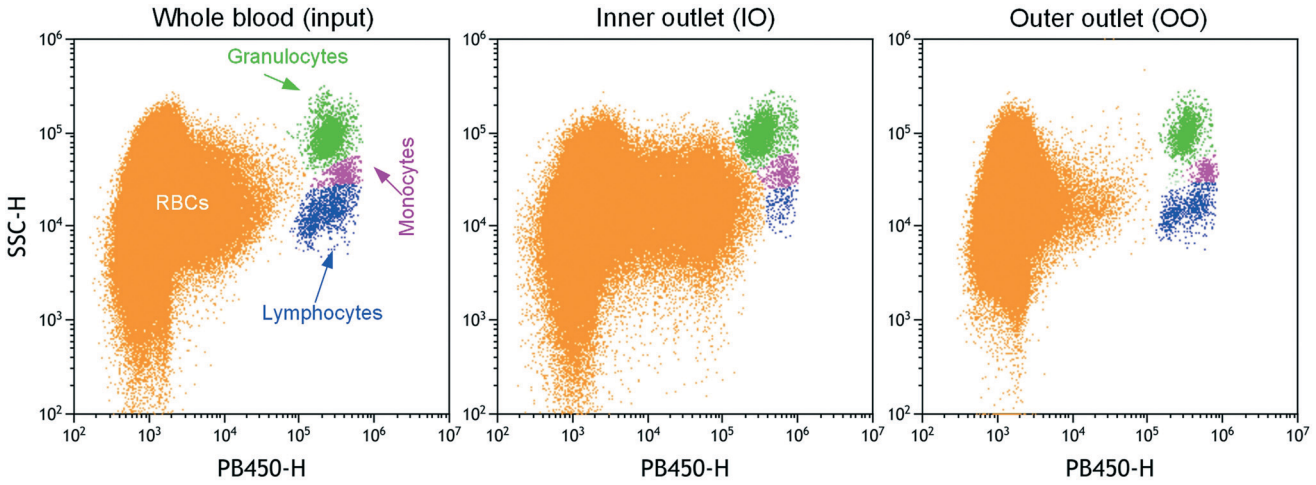

Fig. 10 Representative flow cytometry results of blood cell distributions in whole blood and samples from inner outlet (IO) and outer outlet (OO) after processing through our device. SSC-H and PB450-H represent side scatter-height and Hoechst staining-height, respectively.

neutrophils, eosinophils and basophils increased significantly after flowing through our channel, from 65.3% at input to 87.2% at inner outlet. Conversely, the smaller lymphocytes were reduced from 24.1% down to 4.01%. Accordingly, the percentages of granulocytes and lymphocytes varied in the opposite way at outer outlet (60.2% and 29.4%, respectively). These results solidly confirm the faster migration of the large granulocytes in the blood flow. While WBCs were enriched in our channel at high throughput, the performance in terms of enrichment ratio and WBC purity is not as good as in some of the existing methods that work with highly diluted blood (*e.g.*, pinched flow fractionation,[44] cross-flow filtration,[45] viscoelastic[46,47] and inertial separation[21,48]). The outcome of our system mainly contained RBCs and the performance remains to be further improved.

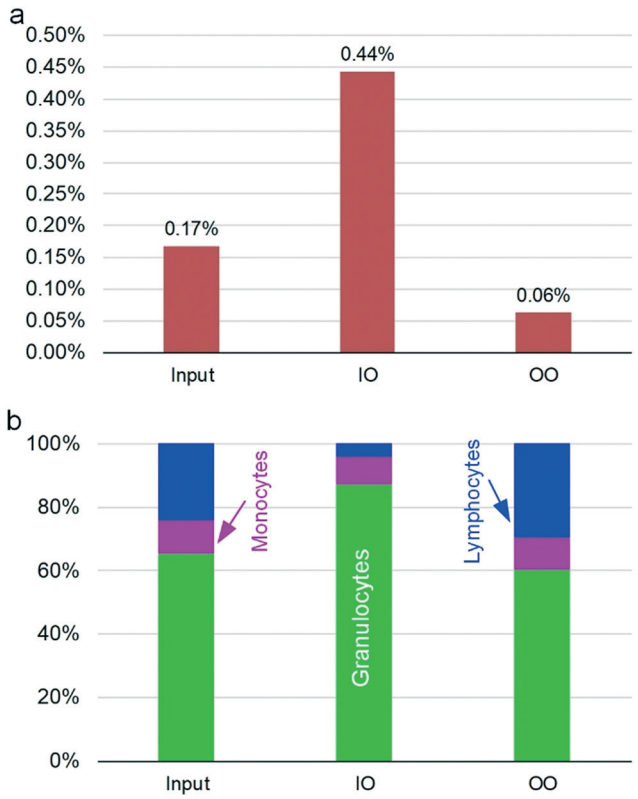

Fig. 11 Variation of WBC and subpopulation percentages before and after processing in microfluidic device. (a) Percent fraction of WBCs in whole blood samples of input, inner outlet (IO) and outer outlet (OO), calculated as the ratio of WBCs over the sum of WBCs and RBCs. (b) Percentage change in WBC subpopulations from input to the two outlets.

Conclusions

In conclusion, we have demonstrated size-dependent lateral migration of particles in whole blood. While particle–particle interactions are generally thought to be detrimental and are to be avoided in microfluidic cell separation systems, it appears that leveraging these interactions can actually lead to preferential migration in whole blood, as corroborated by imaging single-particle trajectories in this work. Larger particles can have lager lateral displacement than smaller ones for a given channel, exhibiting size-dependent migration analogous to the inertial migration. The size-dependent displacement in this work is mainly attributed to the slower velocity of the lager particles in whole blood, which results in longer resident time. The maximum lateral migration velocity is similar for all particle sizes. Nevertheless, smaller particles have a more diverged lateral velocity and migrate slower in general (Fig. 8c). Although viscoelasticity of whole blood may also contribute to the particle displacement, its impact is relatively small as the elasticity of whole blood is generally weak.[38] Further work is required to investigate the role of blood rheology on particle migration.

The prominent yet previously unexpected size-dependent migration of particles and cells within whole blood flow has broad implications in cells sorting applications. First, as

demonstrated herein and our recent work,[34] such fast size-based migration offers a new approach to separation of rare cells with extremely high throughput and operational simplicity. Rare cells, including circulating tumor cells (CTCs) and circulating tumor microemboli (CTM),[22,23] are often larger than blood cells and degrade quickly *in vitro*. Therefore, a rapid processing method with minimal sample preparation (*e.g.*, dilution, cyto/centrifugation, aspiration, and resuspension steps) is highly preferable to harvest such rare events for cancer diagnosis and prognosis.[49,50] Although separation outcome of our previous work was impacted by RBC diffusion, improved understanding of migration dynamics stemming from this work will aid in enhancing separation performance by accounting for migration velocity in the channel design. Specifically, precise control of channel length according to lateral migration velocity can minimize impact of RBC diffusion and reduce resident time of target cells. The side-effect of RBC diffusion may also be overcome by integrating a whole blood separation channel with inertial separation stage since the flow regimes and channel geometries are inherently compatible.

Our results also suggest that permitting cells to preferentially migrate in whole blood toward PBS flow could result in size-dependent separation. For example, WBCs could be separated and enriched from whole blood because of their generally larger size than RBCs (Fig. 10). Separation of target cells directly from untreated whole blood is advantageous as it not only simplifies the workflow and reduces equipment cost, but also serves to reduce cell loss in the sample as compared to conventional centrifugation where 10–30% cell loss is common.[20,51] Moreover, considering the physical size and shape changes in some diseased blood cells (*e.g.*, malaria-infected RBCs[52]), separation of these cells might be possible from whole blood.

Our findings may also improve the understanding of the Zweifach–Fung effect in blood. Under physiological conditions, the volume fraction of blood after blood vessel bifurcation is related to blood flow rate in the daughter vessel: the higher flow rate, the larger volume fraction.[53] This phenomenon is especially useful for plasma extraction.[54,55] It is generally interpreted that this effect results from attraction of particles toward higher-flow-rate vessel.[53] But the exact mechanism remains controversial. Here, we show the size dependent migration of particles and cells could be the result of shear-induced diffusion directed from high-shear-rate region to low-shear-rate region (*i.e.*, from channel walls toward centerline).[34] Although the shear rate exhibits a blunt profile in blood flow, this flat distribution could alter before the vessel bifurcation as flow velocity is reconfigured due to the presence of branch vessels. Faster flow rate means lower shear rate. Hence, all blood cells tend to cross streamlines toward the high-flow-rate side of the vessel before bifurcation. This might contribute to the uneven volume fraction of Zweifach–Fung effect, although flow conditions in the channels are different from those in blood vessels. Nevertheless, our findings may offer insights into the puzzling Zweifach–Fung effect.

Conflicts of interest

There are no conflicts to declare.

Acknowledgements

We gratefully acknowledge partial funding support of the Richard and Loan Hill Department of Bioengineering at the University of Illinois at Chicago and the University of Illinois Cancer Center.

References

1 F. Cui, M. Rhee, A. Singh and A. Tripathi, *Annu. Rev. Biomed. Eng.*, 2015, **17**, 267–286.
2 L. R. Dixon, *J. Perinat. Neonatal Nurs.*, 1997, **11**, 1–18.
3 J. Thiele, K. Bethel, M. Králíčková and P. Kuhn, *Annu. Rev. Pathol.: Mech. Dis.*, 2017, **12**, 419–447.
4 J. Zhang, S. Yan, D. Yuan, G. Alici, N. Nguyen, M. Ebrahimi Warkiani and W. Li, *Lab Chip*, 2016, **16**, 10–34.
5 H. Amini, W. Lee and D. Di Carlo, *Lab Chip*, 2014, **14**, 2739–2761.
6 J. M. Martel and M. Toner, *Annu. Rev. Biomed. Eng.*, 2014, **16**, 371–396.
7 J. Gao, R. Riahi, M. L. Sin, S. Zhang and P. K. Wong, *Analyst*, 2012, **137**, 5215–5221.
8 J. H. Kang, S. Krause, H. Tobin, A. Mammoto, M. Kanapathipillai and D. E. Ingber, *Lab Chip*, 2012, **12**, 2175–2181.
9 P. Augustsson, C. Magnusson, M. Nordin, H. Lilja and T. Laurell, *Anal. Chem.*, 2012, **84**, 7954–7962.
10 M. P. MacDonald, G. C. Spalding and K. Dholakia, *Nature*, 2003, **426**, 421–424.
11 L. R. Huang, E. C. Cox, R. H. Austin and J. C. Sturm, *Science*, 2004, **304**, 987–990.
12 J. McGrath, M. Jimeneza and H. Bridle, *Lab Chip*, 2014, **14**, 4139–4158.
13 M. Yamada, M. Nakashima and M. Seki, *Anal. Chem.*, 2004, **76**, 5465–5471.
14 A. A. S. Bhagat, H. W. Hou, L. D. Li, C. T. Lim and J. Han, *Lab Chip*, 2011, **11**, 1870–1878.
15 M. Yamada and M. Seki, *Lab Chip*, 2005, **5**, 1233–1239.
16 N. Pamme, *Lab Chip*, 2007, **7**, 1644–1659.
17 J. Nam, H. Lim, D. Kim, H. Jung and S. Shin, *Lab Chip*, 2012, **12**, 1347–1354.
18 C. Liu, C. Xue, X. Chen, L. Shan, Y. Tian and G. Hu, *Anal. Chem.*, 2015, **87**, 6041–6048.
19 C. Tu, J. Zhou, Y. Liang, B. Huang, Y. Fang, X. Liang and X. Ye, *Biomed. Microdevices*, 2017, **19**, 83.
20 M. E. Warkiani, G. Guan, K. B. Luan, W. C. Lee, A. A. S. Bhagat, P. Kant Chaudhuri, D. S. Tan, W. T. Lim, S. C. Lee, P. C. Y. Chen, C. T. Lim and J. Han, *Lab Chip*, 2014, **14**, 128–137.
21 N. Nivedita and I. Papautsky, *Biomicrofluidics*, 2013, **7**, 054101.
22 J. Zhou, A. Kulasinghe, A. Bogseth, K. O'Byrne, C. Punyadeera and I. Papautsky, *Microsyst. Nanoeng.*, 2019, **5**, 8.

23 A. Kulasinghe, J. Zhou, L. Kenny, I. Papautsky and C. Punyadeera, *Cancers*, 2019, **11**, 89.
24 S. S. Shevkoplyas, T. Yoshida, L. L. Munn and M. W. Bitensky, *Anal. Chem.*, 2005, **77**, 933–937.
25 A. Jain and L. L. Munn, *Lab Chip*, 2011, **11**, 2941–2947.
26 X. Li, W. Chen, G. Liu, W. Lu and J. Fu, *Lab Chip*, 2014, **14**, 2565–2575.
27 Y. Cheng, X. Ye, Z. Ma, S. Xie and W. Wang, *Biomicrofluidics*, 2016, **10**, 014118.
28 J. A. Davis, D. W. Inglis, K. J. Morton, D. A. Lawrence, L. R. Huang, S. Y. Chou, J. C. Sturm and R. H. Austin, *Proc. Natl. Acad. Sci. U. S. A.*, 2006, **103**, 14779–14784.
29 J. Choi, J. C. Hyun and S. Yang, *Sci. Rep.*, 2015, **5**, 15167.
30 M. G. Lee, J. H. Shin, C. Y. Bae, S. Choi and J. Park, *Anal. Chem.*, 2013, **85**, 6213–6218.
31 B. Kim, Y. J. Choi, H. Seo, E. Shin and S. Choi, *Small*, 2016, **12**, 5159–5168.
32 E. S. Park, C. Jin, Q. Guo, R. R. Ang, S. P. Duffy, K. Matthews, A. Azad, H. Abdi, T. Todenhöfer, J. Bazov, K. N. Chi, P. C. Black and H. Ma, *Small*, 2016, **12**, 1909–1919.
33 Google Patents. *Pat.*, US20170296732A1.
34 J. Zhou, C. Tu, Y. Liang, B. Huang, Y. Fang, X. Liang, I. Papautsky and X. Ye, *Sci. Rep.*, 2018, **8**, 9411.
35 M. E. Warkiani, B. L. Khoo, L. Wu, A. K. P. Tay, A. A. S. Bhagat, J. Han and C. T. Lim, *Nat. Protoc.*, 2016, **11**, 134–148.
36 J. Zhou and I. Papautsky, *Lab Chip*, 2013, **13**, 1121–1132.
37 J. Zhou, P. V. Giridhar, S. Kasper and I. Papautsky, *Lab Chip*, 2013, **13**, 1919–1929.
38 G. B. Thurston and N. M. Henderson, *Biorheology*, 2006, **43**, 729–746.
39 D. Yuan, J. Zhang, S. Yan, G. Peng, Q. Zhao, G. Alici, H. Du and W. Li, *Electrophoresis*, 2016, **37**, 2147–2155.
40 D. Yuan, S. H. Tan, R. Sluyter, Q. Zhao, S. Yan, N. Nguyen, J. Guo, J. Zhang and W. Li, *Anal. Chem.*, 2017, **89**, 9574–9582.
41 F. Tian, L. Cai, J. Chang, S. Li, C. Liu, T. Li and J. Sun, *Lab Chip*, 2018, **18**, 3436–3445.
42 D. Leighton and A. Acrivos, *J. Fluid Mech.*, 1987, **181**, 415–439.
43 M. Roussel, C. Benard, B. Ly-Sunnaram and T. Fest, *Cytometry, Part A*, 2010, **77**, 552–563.
44 C. Cupelli, T. Borchardt, T. Steiner, N. Paust, R. Zengerle and M. Santer, *Microfluid. Nanofluid.*, 2013, **14**, 551–563.
45 J. Alvankarian, A. Bahadorimehr and B. Yeop Majlis, *Biomicrofluidics*, 2013, **7**, 014102.
46 J. Nam, J. Yoon, J. Kim, W. S. Jang and C. S. Lim, *J. Chromatogr. A*, 2019, **1595**, 230–239.
47 J. K. Tan, S. Park, H. L. Leo and S. Kim, *IEEE Trans. Biomed. Circuits Syst.*, 2017, **11**, 1431–1437.
48 L. Wu, G. Guan, H. W. Hou, A. A. S. Bhagat and J. Han, *Anal. Chem.*, 2012, **84**, 9324–9331.
49 M. May, *Science*, 2016, **351**, 300–302.
50 J. Kaiser, *Science*, 2010, **327**, 1072–1074.
51 X. Tong, L. Yang, J. C. Lang, M. Zborowski and J. J. Chalmers, *Cytometry, Part B*, 2007, **72**, 310–323.
52 H. W. Hou, A. A. S. Bhagat, A. G. Chong, P. Mao, K. S. Tan, J. Han and C. T. Lim, *Lab Chip*, 2010, **10**, 2605–2613.
53 V. Doyeux, T. Podgorski, S. Peponas, M. Ismail and G. Coupier, *J. Fluid Mech.*, 2011, **674**, 359–388.
54 S. Yang, A. Ündar and J. D. Zahn, *Lab Chip*, 2006, **6**, 871–880.
55 Z. Fekete, P. Nagy, G. Huszka, F. Tolner, A. Pongrácz and P. Fürjes, *Sens. Actuators, B*, 2012, **162**, 89–94.

